Acoustic vortex in a waveguide with a chiral gradient sawtooth metasurface

Zeliang Song,[1] Shuhuan Xie,[2] Hua Ding,[2] Feiyan Cai,[3] Yugui Peng,[1] Xuefeng Zhu,[1] Yong Li,[2,*] and Degang Zhao[1,†]

[1] *Department of Physics, Huazhong University of Science and Technology, Wuhan 430074, China*
[2] *Institute of Acoustics, School of Physics Science and Engineering, Tongji University, Shanghai 200092, China*
[3] *Paul C. Lauterbur Research Center for Biomedical Imaging, Shenzhen Institutes of Advanced Technology, Chinese Academy of Sciences, Shenzhen 518055, China*

(Received 24 July 2023; revised 23 April 2024; accepted 3 May 2024; published 4 June 2024)

Acoustic vortex states with spiral phase dislocation that can carry orbital angular momentum (OAM) have aroused much research interest in recent years. The mainstream methods of generating acoustic vortexes are based on the Huygens-Fresnel principle to modulate the wave front to create spatial spiral phase dislocation. In this work, we realize acoustic vortexes in a waveguide with a chiral gradient sawtooth metasurface. The physical mechanism of our method is to lift the degenerate dipole eigenmodes through the scattering effect of the chiral surface structure, and then their superposition yields both $+1$ and -1 order vortexes. Compared with the existing methods of acoustic vortex generation, our design has many merits. For instance, it is easy to manufacture and control, the working frequency is relatively broadband, and the sign of vortex order can be readily flipped. Both the full-wave simulations and experimental measurements validate the existence of the acoustic vortexes. The torque effect of the acoustic vortexes is also successfully performed by rotating a foam disk as a practical application. Our work opens a new route for generating acoustic vortex and could have potential significance in areas including microfluidics, acoustic tweezers, and ultrasonic communication.

DOI: 10.1103/PhysRevApplied.21.064006

I. INTRODUCTION

Sound waves with orbital angular momentum (OAM), called an acoustic vortex, have launched a brand new approach for controlling acoustic waves, which has aroused a lot of research interest. The pressure field of the acoustic vortex behaves with a helicoidal phase dependence in its wave front, which can be described by a phase term $e^{il\varphi}$, where l is the topological charge or the order of the vortex, representing the number of twists in a wavelength along the propagation direction or the number of 2π phase cycles around a closed path in the wave front. The concept of this kind of phase dislocation was initially proposed by Nye and Berry as early as 1974 [1]. An acoustic vortex contains a phase singularity (where the phase becomes indeterminate) at the center axis, accompanied by a null pressure magnitude [1–3]. This peculiar characteristic can be used in noncontact particle manipulation, such as particle trapping [4–16]. On the other hand, the acoustic vortex wave front can exert torque on the sound-absorbing objects positioned on the propagation path. This torque effect can be used for noncontact rotation manipulation [17–28]. In addition, the distinct topological charges of OAM provide orthogonal channels that serve as an extra independent degree of freedom in transmitting information. Therefore, the acoustic vortex has the potential capability of acoustic communication through encoding information onto the vortex waves [29–33].

Over the past two decades, some significant achievements have emerged for generating acoustic vortexes. These methods can generally be classified into two types: active and passive. The active method refers to a straightforward production of the helicoidal phase by using a phase-controllable sound source array, which was first proposed in Hefner and Marston's pioneer work using four-panel transducers with gradient-varied phases [2,3]. Since then, high-quality acoustic vortex beams can be generated by using state-of-the-art transducer arrays applying increasing numbers of transducers and exactly presetting each transducer's phase and amplitude, which are precisely controlled by digital processors [4–7,17–20,33–39]. In essence, the underlying physics is the Huygens-Fresnel principle. Technically speaking, the active method can efficiently generate acoustic vortexes for any topological charge and any allowed frequencies. Nonetheless, the cost of a large number of transducers is very high and the control system is inevitably complicated. The passive method, generally speaking, refers to modulating the sound field with well-designed artificial structures. For

*Corresponding author: yongli@tongji.edu.cn
†Corresponding author: dgzhao@hust.edu.cn

example, when a sound plane wave passes through well-designed artificial microstructures, its uniform phase on the wave front can be dislocated into a spatial helical distribution. The passive technology was first realized using structures with helical dislocation surfaces [40,41]. Subsequently, a variety of inventive and ingenious designs have been proposed and developed, such as Helmholtz resonator-based metasurfaces [21,22,42–44], spiral diffraction gratings [10,45–49], and acoustic holographic lenses [50,51]. In addition, some other mechanisms are employed to induce acoustic vortexes, such as utilizing a noncoaxial waveguide to twist the output acoustic wave [52], introducing chiral non-Hermitian modulation in a parity-time-symmetric ring cavity [53], and modulating the wave via metagrating to attain acoustic spatiotemporal vortexes in frequency-momentum space [54,55]. However, the topology architectures of the above passive structures heavily depend on the working frequency and, generally, one structure has only one working frequency instead of a frequency range.

In this work, we report an essentially distinct method for generating acoustic vortexes using a single sound source in a cylindrical waveguide, which is designed with sawtoothlike grooves that are evenly distributed along the circumferential direction on the surface. These azimuthal gradient grooves can remove the degeneracy of the waveguide's eigenmodes, which enables them to have a different wave number k_z in the propagation direction at the same excited frequency. Owing to the difference in the growth of the phase term $e^{-ik_z z}$, the superposition of the two degeneracy lifted modes can form vortex fields wherever their phase difference equals an odd number times $\pi/2$. Consequently, in a wide frequency region, a vortex wave field with a spatial-dependent topological charge $l = \pm 1$ can be generated and the topological charge can be readily flipped by adjusting the position of the sound source on the incident plane, which are demonstrated by a full-wave simulation obtained using the finite-element solver COMSOL MULTIPHYSICS and verified by experimental measurements. Furthermore, to visually exhibit the acoustic vortex field, we show the torque effect on an absorbing foam disk due to the transferring of OAM from a vortex field to matter. Our work presents a unique mechanism that relies on the superposition of chiral waveguide's eigenmodes to generate an acoustic vortex field, providing a new line of thinking in designing economical, relatively broadband, multifunctional acoustic vortex devices.

II. DEGENERACY LIFTING OF DIPOLE MODES IN WAVEGUIDE WITH CHIRAL GRADIENT SAWTOOTH METASURFACE

To begin, we consider a typical solid and infinitely long circular-cylindrical waveguide of radius $r_0 = 40$ mm filled with air, as shown in Fig. 1(a). By solving the Helmholtz equation in cylindrical coordinates (r, φ, z), the sound pressure eigensolutions can be expressed as [56–58]

$$p_{mn} = J_m(k_{mn}r)(A_m \cos m\varphi + B_m \sin m\varphi)e^{-ik_z z}, \quad (1)$$

where $J_m(k_{mn}r)$ is the first-kind Bessel function of mth order ($m \geq 0$). Moreover, k_{mn} is the in-plane wave vector component, which can be determined by the Neumann boundary condition $[\partial J_m(k_{mn}r)/\partial r]_{r=r_0} = 0$, where n denotes the nth root. It satisfies $k_{mn}^2 + k_z^2 = \omega^2/c^2$, where $\omega = 2\pi f$ is the angular frequency, k_z refers to the propagation wave vector component along the z-axis, and $c = 343$ m/s is the sound velocity in air. Then, each eigenmode can be labeled by two integers (m, n).

The dispersion relation (the relation between the eigenfrequency and k_z) of this cylindrical waveguide is depicted in Fig. 1(b). The lowest straight line represents the $(0, 0)$ mode satisfying $\omega = ck_z$ and it is actually the plane wave component $A_0|p_0\rangle = A_0 e^{-ik_z z}$. Its pressure field is uniformly distributed in the transverse plane, which is known as the monopole mode [see the inset of Fig. 1(b)]. The second curve represents the $(1, 0)$ mode, whose cutoff frequency is $ck_{10}/2\pi = 1.841c/2\pi r_0 = 2512$ Hz, which can be determined exactly by solving the boundary condition [56–58]. As shown in Fig. 1(c), the field distribution clearly reveals that they are two orthogonal dipole modes [38,52,59]. Henceforth, we mainly focus on the $(1, 0)$ mode and the dispersion curves of higher-order modes are given in Supplemental Material S1 [60]. However, in the circular waveguide, a vortex mode cannot be generated by a common sound source such as a plane wave or single monopole source directly, because the two definitely degenerate dipole modes have no phase difference and their superposition cannot bring about the gradient phase term $e^{il\varphi}$. This is why previous works must utilize a well-designed sound source array or artificial microstructures to produce a phase gradient intentionally [38,39,42,63].

It is natural to ask the question: can these two degenerate modes be lifted? Geometrically, the degeneracy feature of the dipole eigenmodes originates from the spatial inversion symmetry in the azimuthal direction. If an artificial structure is elaborately designed on the surface to break this symmetry, it is anticipated that the degeneracy can be lifted. On these grounds, we carve 12 grooves with a gradient size on the surface of the circular waveguide to break the circumferential symmetry, as shown in Fig. 1(d). The depth of the grooves is $r_2 - r_1 = 10$ mm, which is about one order of magnitude smaller than the working wavelength. Then, this groove structure can act as a metasurface. The central angle of each convex-concave pair is fixed at 30°, while the central angles of the convex parts linearly increase counterclockwise from $\theta_1 = 6°$ to $\theta_{12} = 17°$ with steps of 1°. The numerically calculated dispersion relation and eigenfield distributions of pressure are presented in Figs. 1(e) and 1(f), respectively. It is obvious

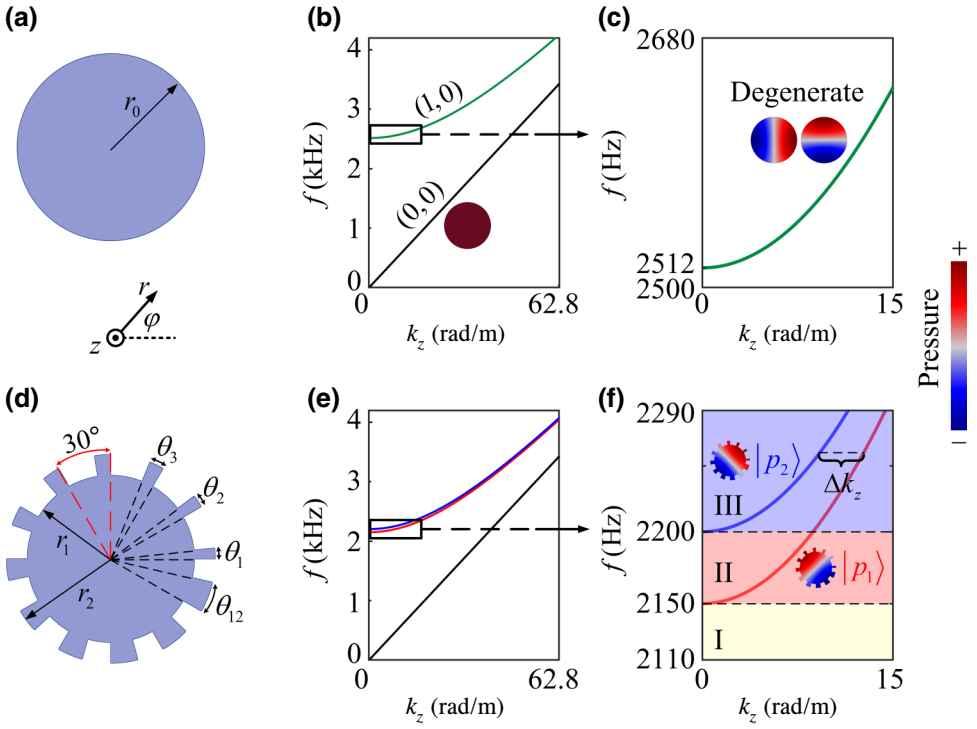

FIG. 1. Eigenmodes analysis and degeneracy splitting. (a) Sectional view of the circular waveguide, with radius $r_0 = 40$ mm. The waveguide is infinitely long in the z-direction. (b) Dispersion relations of the two lowest-order eigenmodes of the circular waveguide. The inset is the pressure eigenfield distribution of the $(0, 0)$ mode. (c) Magnified view of the dispersion relation of the $(1, 0)$ mode in (b). The insets are the pressure eigenfield distributions of the doubly degenerate $(1, 0)$ mode. (d) Sectional view of the waveguide with a chiral gradient sawtooth metasurface. All grooves are homocentric fans, with an inner radius $r_1 = 40$ mm and outer radius $r_2 = 50$ mm. The structure consists of 12 pairs of grooves in total. The central angle of each convex-concave pair is fixed at 30°, whereas that of the convex part follows the function $\theta_i = \theta_1 + (i - 1)\delta$, $i = 1, 2, \ldots, 12$ with $\theta_1 = 6°$ and $\delta = 1°$. (e) Dispersion relations of the three lowest-order eigenmodes of the waveguide with the cross-section shown in (d). (f) Magnified view of the degeneracy lifted modes in (e). The insets are the pressure eigenfield distributions of $|p_1\rangle$ and $|p_2\rangle$ modes at the cutoff frequencies. At a certain frequency above the higher cutoff frequency 2200 Hz, the horizontal interval of the two dispersion curves denotes the difference for k_z, i.e., $\Delta k_z = k_{1z} - k_{2z}$.

that the original two degenerate dipole modes split into two distinguishable modes. The new cutoff frequencies are $f_1 = 2150$ Hz and $f_2 = 2200$ Hz, respectively. These two degeneracy lifted eigenmodes can be approximatively expressed as

$$\begin{aligned} |p_1\rangle &\approx J_1(k_{1r}r)e^{-ik_{1z}z}\sin(\varphi - \varphi_0)\,, \\ |p_2\rangle &\approx J_1(k_{2r}r)e^{-ik_{2z}z}\cos(\varphi - \varphi_0), \end{aligned} \tag{2}$$

where $\varphi_0 = 44°$ determines the polarization direction of the dipole modes. It should be pointed out that these degeneracy lifted modes have a definite φ_0, whereas the degenerate modes in the circular waveguide φ_0 can be any value [58], and we set $\varphi_0 = 0$ in Fig. 1(c) for simplicity. The patterns of the eigenfield distributions in the transverse plane for $|p_1\rangle$ and $|p_2\rangle$ modes, as shown in the insets of Fig. 1(f), are nearly unchanged compared with the degenerate modes in the circular waveguide, exhibiting only a small deviation near the boundary. Then, the approximation in Eq. (2) is absolutely valid (see Supplemental Material S2 [60]). In principle, the chiral gradient sawtooth metasurface effectively introduces small perturbation that successfully lifts the two degenerate modes while preserving their wave function relation. A similar phenomenon is analytically frequently encountered in quantum systems, which can be solved by well-established degenerate perturbation theory.

III. REALIZATION OF AN ACOUSTIC VORTEX WITH DEGENERACY LIFTED MODES

The lifting of the degeneracy divides the frequency domain into three zones, which are revealed by different color-filled regions in Fig. 1(f). A sound source with a frequency in Zone I will only excite the monopole mode $|p_0\rangle$. In Zone II, the dipole mode $|p_1\rangle$ can be excited and it coexists with the monopole mode. In Zone III, $|p_1\rangle$, $|p_2\rangle$, and the monopole mode can be excited simultaneously because the excited frequency exceeds f_2 (here, the working frequency

is limited below the cutoff frequency of the eigenmode, i.e., higher than $|p_2\rangle$, to avoid exciting higher-order eigenmodes). Consequently, the pressure field in any position of the waveguide can be expressed as the linear superposition of eigenmodes $|p\rangle = A_0|p_0\rangle + A_1|p_1\rangle + A_2|p_2\rangle$. Through an ingenious design (see Supplemental Material S3 [60]), the acoustic vortex can be generated when two essential conditions are satisfied, which are given as follows:

$$\begin{aligned} &(a)\ \text{Amplitude condition } |A_1 J_1(k_{1r}r)| = |A_2 J_1(k_{2r}r)| = A, \\ &(b)\ \text{Phase difference condition } \Delta k_z z = (k_{1z} - k_{2z})z = (2N-1)\pi/2, \quad N \in \mathbb{N}. \end{aligned} \tag{3}$$

For example, assuming $-A_1 J_1(k_{1r}r) = A_2 J_1(k_{2r}r) = A$ satisfies condition (a) and $\Delta k_z z = \pi/2$ satisfies condition (b), the superposition of states $|p_1\rangle$ and $|p_2\rangle$ is

$$\begin{aligned} A_1|p_1\rangle + A_2|p_2\rangle &= A_1 J_1(k_{1r}r)\sin(\varphi-\varphi_0)e^{-ik_{1z}z} + A_2 J_1(k_{2r}r)\cos(\varphi-\varphi_0)e^{-ik_{2z}z} \\ &= Ae^{-ik_{2z}z}[-e^{-i\Delta k_z z}\sin(\varphi-\varphi_0) + \cos(\varphi-\varphi_0)] \\ &= Ae^{-ik_{2z}z}[i\sin(\varphi-\varphi_0) + \cos(\varphi-\varphi_0)] \\ &= Ae^{i(-k_{2z}z+\varphi-\varphi_0)}. \end{aligned} \tag{4}$$

The gradient phase term $e^{i\varphi}$ in Eq. (4) indicates the helical phase distribution and a vortex mode with topological charge $l = +1$ has been produced successfully. It should be noted that although the monopole mode $|p_0\rangle$ coexists, fortunately its field is uniformly distributed in the wave front and does not provide any in-plane phase gradient but only acts as a background.

In principle, the amplitude condition Eq. 3(a) depends on the modal amplitudes A_1 and A_2 or, in other words, the relative weights of modes $|p_1\rangle$ and $|p_2\rangle$. A simple plane wave source should be located off-center, and the modal amplitudes can be readily adjusted only by tuning the azimuthal angle φ_s of the source. A detailed mathematical derivation is presented in Supplemental Material S3 [60]. The phase difference condition Eq. 3(b) relies on Δk_z (determined by the dispersion relation) and the propagation distance z from the incident plane.

To demonstrate our strategy for creating the acoustic vortex, we fabricated the waveguide samples according to the parameters in Fig. 1(d) via stereolithographic 3D printing technology, as exhibited in Fig. 2(a). The raw material of the sample is photosensitive resin and its wall thickness is $d = 3$ mm, which guarantees the hard boundary condition. As is shown in Fig. 2(b), a loudspeaker with a diameter of about 16 mm is positioned off-center in the input port, with the offset distance of about $r_s = 25$ mm. The loudspeaker is embedded in a sound-absorbing foam plate [see Fig. 2(b)], which is used to fix the position of the loudspeaker, whereas the azimuthal angle of the loudspeaker can be easily adjusted by rotating the plate manually. The output port of the waveguide is fully filled by more sound-absorbing foam to play the role of a perfectly matched layer. A 1/8-inch microphone (Brüel & Kjær 4138-A-015), tied to a long, specially made auxiliary steel rod, is horizontally moved into the waveguide to scan the sound field.

Here, we choose the working frequency of 2330 Hz, which entails $\Delta k_z = 2.58$ rad/m in terms of the dispersion relations [Fig. 1(e)]. Firstly, we set the azimuthal angle of the sound source as $\varphi_s = -7^\circ$, which satisfies $-A_1 J_1(k_{1r}r) = A_2 J_1(k_{2r}r)$ and, moreover, the examined plane is chosen as $z = 0.61$ m, which satisfies $\Delta k_z z = \pi/2$. This setting will produce a $+1$ order pure acoustic vortex, as discussed previously in Eq. (4). The phase distributions in the simulation and experiment are exhibited in Figs. 2(c) and 2(f), respectively. They closely match and clearly show that the phase increases counterclockwise along the azimuthal direction with a 2π jump for one annular loop, revealing a vortex mode with $l = +1$. Next, we adjust φ_s to 95° so that the amplitude condition becomes $A_1 J_1(k_{1r}r) = A_2 J_1(k_{2r}r)$, while keeping the position of the examined plane unchanged. Using the derivation similar to Eq. (4), a phase term $e^{-i\varphi}$ appears, implying a -1 order acoustic vortex has been produced. The well-matched simulated [Fig. 2(d)] and experimental [Fig. 2(g)] phase distributions perfectly demonstrate the existence of -1 order vortex: the phase clockwise increases 2π over one annular loop. At the same frequency, the acoustic vortex can also be obtained at different positions on the z-axis. For instance, we fix $\varphi_s = -7^\circ$, i.e., $-A_1 J_1(k_{1r}r) = A_2 J_1(k_{2r}r)$, the same as the example in Eq. (4), but the examined plane is changed at $z = 1.83$ m,

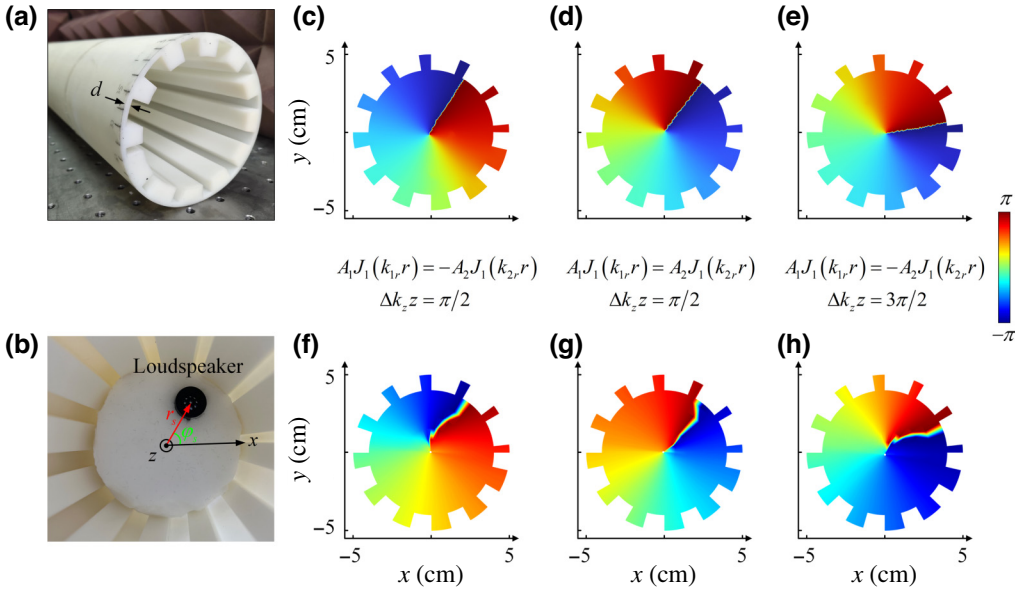

FIG. 2. Phase distribution of the acoustic vortex. (a) Photograph of the fabricated waveguide sample. (b) Experimental setup of the loudspeaker. (c)–(h) Phase distribution of the acoustic vortex for the three cases obtained by the (c)–(e) numerical simulation and (f)–(h) experimental measurement. The parameter settings for the three cases are: (c),(f) $\varphi_s = -7^\circ$, $z = 0.61$ m; (d),(g), $\varphi_s = 95^\circ$, $z = 0.61$ m; (e),(h) $\varphi_s = -7^\circ$, $z = 1.83$ m. The working frequency is fixed at 2330 Hz.

which satisfies $\Delta k_z z = 3\pi/2$. Then, calculating $A_1|p_1\rangle + A_2|p_2\rangle$ yields a $e^{-i\varphi}$ phase term, resulting in the creation of a vortex with a topological charge of -1. The phase distributions in this case resemble those shown in Figs. 2(d) and 2(g), and the numerical simulation [Fig. 2(e)] effectively agrees with the experimental measurement [Fig. 2(h)]. Certainly, the vortex mode can also exist at the position that satisfies $\Delta k_z z = 5\pi/2, 7\pi/2, 9\pi/2, \cdots$. However, in practice, obtaining high-quality vortexes at distances too distant from the source is challenging due to the inevitable dissipation of the propagating acoustic wave.

To characterize the quality of the vortex,

$$Q = \frac{\mathrm{Im}\,\langle p|\,\partial_\varphi|p\rangle}{\langle p|\,p\rangle} \tag{5}$$

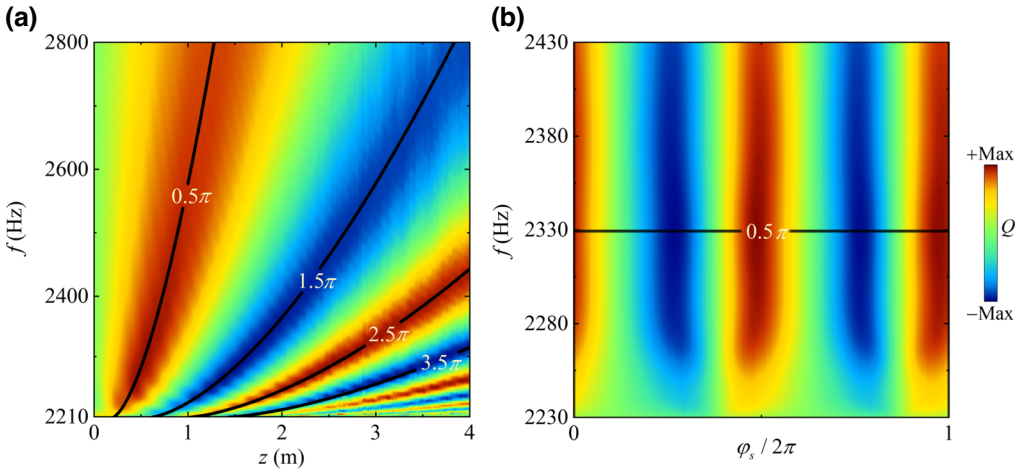

FIG. 3. Quality of the vortex. (a) The Q factor of the vortex states versus frequency and z coordinate of the examined plane, with the sound source fixed at $\varphi_s = -7^\circ$. The red and blue colors denote the $+1$ and -1 order vortex, respectively. (b) The Q factor of the vortex states versus frequency and the azimuthal angle φ_s of the sound source, with the examined plane fixed at $z = 0.61$ m. The solid curves are plotted according to the phase difference condition Eq. 3(b), and the numbers in the curves denote the quantity of $\Delta k_z z$.

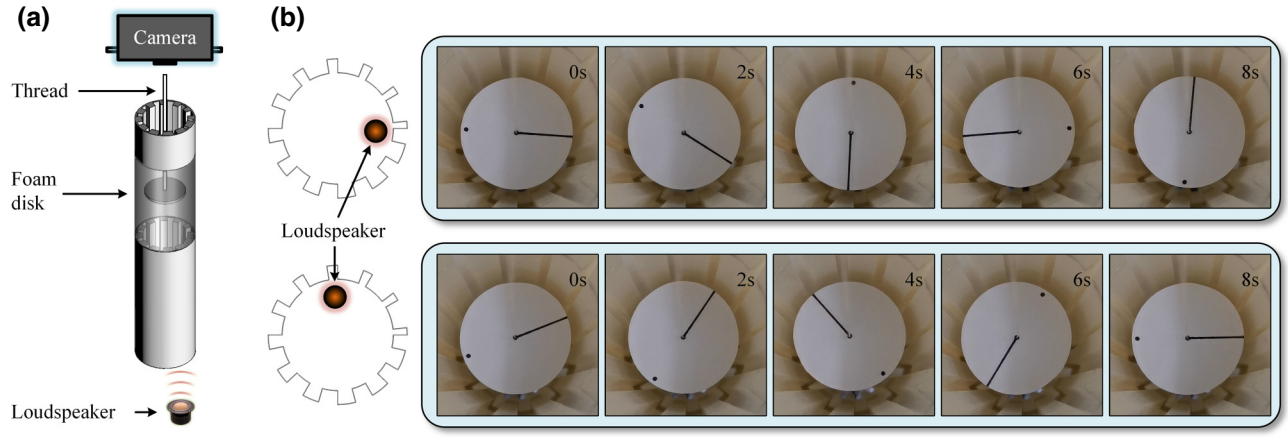

FIG. 4. Torque effect of the acoustic vortex exerted on an absorbing foam disk. (a) Schematic diagram of the experimental setup. (b) Snapshots of the rotational motion of the foam disk at different time points. The foam disk is positioned at a distance $z = 0.61$ m from the incident plane. A black line segment is marked for the observation of the disk rotation. The loudspeaker is positioned at $\varphi_s = -7^\circ$ (top) and $\varphi_s = 95^\circ$ (bottom) and, consequently, the foam disk rotates clockwise (top) and counterclockwise (bottom).

can be defined [64,65], which essentially indicates the expectation value of the OAM in the state $|p\rangle$. In Fig. 3(a), we numerically calculate the Q factor with respect to frequency and z coordinate of the examined plane, with the sound source fixed at $\varphi_s = -7^\circ$. The vortexes with the best qualities are located on the curves calculated by $\Delta k_z z = (2N-1)\pi/2$, $N \in \mathbb{N}$, i.e., the phase difference condition Eq. 3(b), whereas the quality of the vortex declines a distance from the curves. Obviously, in our design, only one waveguide sample can achieve high-quality vortexes in a relatively wide frequency region compared with some present passive structures with only a single working frequency. According to Fig. 3(a), high-quality vortexes can be obtained at different z positions for both $+1$ (red region) and -1 (blue region) orders at different frequencies. Figure 3(b) presents the Q factor calculated in the transverse plane at $z = 0.61$ m versus the frequency and the azimuthal angle φ_s of the sound source. Similar to Fig. 3(a), the vortex states with the best qualities are located on the line $\Delta k_z z = \pi/2$. In a 2π period of φ_s, the Q factor exhibits a cyclical variation, and the sign of the topological charge of vortex flips every $\pi/2$ change of φ_s. This periodicity originates from the periodic functional relationship of the relative weights of $|p_1\rangle$ and $|p_2\rangle$ with respect to φ_s, which has been demonstrated in Supplemental Material S3 [60].

IV. EXPERIMENTAL DEMONSTRATION OF THE TORQUE EFFECT

One fantastic effect of acoustic vortex is that the spiral field can transfer OAM to a sound-absorbing object, which is known as the vortex-induced torque effect [18,21–24]. Here, we experimentally demonstrate this torque effect by noncontact rotating a light object. As schematically shown in Fig. 4(a), a loudspeaker (with radius 35 mm) is positioned off-centered at the bottom of a waveguide to act as

VIDEO 1. Clockwise rotation of the foam disk. This reveals the torque effect of an excited $+1$ order acoustic vortex. The vortex transfers the OAM from the wave to the foam disk, and then the foam disk rotates clockwise.

VIDEO 2. Counterclockwise rotation of the foam disk. This reveals the torque effect of an excited -1 order acoustic vortex. The vortex transfers the OAM from the wave to the foam disk, and then the foam disk rotates counterclockwise.

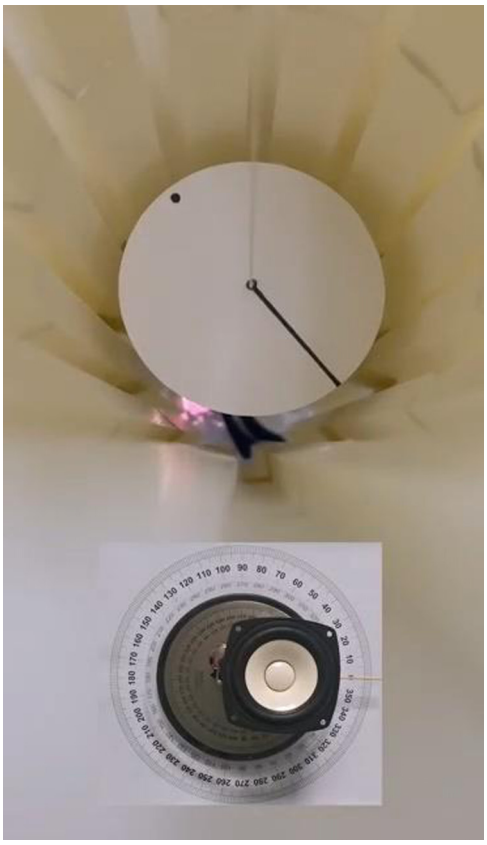

VIDEO 3. Switch between the clockwise and counterclockwise rotation of the foam disk. As Fig. 3(b) shows, the sign of the acoustic vortex order can be readily tuned by adjusting the angular position of the off-centered sound source. When we continuously change the angular position of the loudspeaker in a 2π period, the sign of acoustic vortex order flips four times. Obviously, the rotational direction of the foam disk also flips four times.

the sound source, with a working frequency of 2330 Hz. A light, sound-absorbing foam disk is hung 0.61 m above the loudspeaker. A camera is fixed above the foam disk to record videos. First, the loudspeaker is placed at $\varphi_s = -7^\circ$ and, as soon as the sound is launched from the loudspeaker, the foam disk starts rotating clockwise, as is shown in the top row of Fig. 4(b), due to a $+1$ order vortex. Video 1 displays the rotational motion of the disk. Here, the selected hang thread (sewing thread) has a very small shear modulus; thus, it produces a very small torque when it is twisted. Therefore, the disk can continuously rotate for a very long time. As is discussed in Fig. 3(b), the topological charge of the vortex can easily be flipped by tuning the azimuthal angle of the sound source. Then, we place the loudspeaker at $\varphi_s = 95^\circ$, and, unsurprisingly, the disk rotates counterclockwise due to the fact that a -1 order vortex has been excited, which is clearly illustrated in the bottom row of Fig. 4(b) as well as in Video 2. In addition, we fixed the loudspeaker onto a turntable and rotated it one full cycle. It intuitively shows that the rotational direction of the disk flips four times, which is displayed in Video 3.

V. CONCLUSION

In this work, we have presented an innovative approach to generating an acoustic vortex in a cylindrical waveguide with a chiral gradient sawtooth metasurface. The chiral structure has been used to split the degenerate dipole eigenmodes. The superposition of these two orthogonal modes produces ± 1 order acoustic vortexes, assuming they satisfy two essential conditions: an amplitude condition and a phase difference condition. The measurement of the phase distribution and torque effect experiment exactly verify the validity of our theory. The key point of our method is the lifting of the degeneracy of the multipole eigenmodes, which is achieved by the scattering effect of the acoustic wave on the chiral metasurface structure. Certainly, the configuration of chiral gradient metasurface structure is not unique. Other kinds of surface design may realize similar effects. However, the architecture of the metasurface structure should be designed very carefully: it should not extensively break the functional relations of dipole modes,

i.e., Eq. (2) should be satisfied, and, simultaneously, the two dipole modes should have a sufficient difference for the propagating wave number Δk_z. In this work, if the size of the sawtooth is too large or the gradient size is too great, although the wave number difference Δk_z may become wider, the dipole property of the eigenmodes may be significantly distorted by the strong wave scattering on the surface and a high-quality vortex cannot be obtained.

Although it is well-known that the acoustic wave is a longitudinal wave, the acoustic dipole modes in the waveguide have some characteristics of transverse waves: they have wave vector components k_r, which are perpendicular to the propagation direction [38,56]. From this point of view, the two orthogonal dipole modes $|p_1\rangle$ and $|p_2\rangle$ can be analogized as the TE and TM modes in optics. Then, the physical mechanism of the generating acoustic vortex in our work is similar to the generation of circularly polarized light: passing a linearly polarized light through a quarter-wave plate at an angle of 45° to the optic axis of the plate.

In contrast to conventional methods for generating sound vortexes that rely on complex electronic control or intricate craftmanship, our design offers many advantages. For instance, our structure is simple and easy to fabricate, and we only use one waveguide and one loudspeaker to generate vortexes in relatively broadband frequency regions. According to the phase difference condition, the vortexes of different frequencies can be obtained in the transverse plane at different distances from the sound source. In terms of the amplitude condition, the sign of the topological charge and the quality of the vortex can be flexibly tuned through adjusting the angular position of the sound source. Our study provides a fresh perspective on generating a sound vortex and is potentially significant in various practical applications, including but not limited to a micromixer in microfluidic systems, noncontact manipulation of small objects in biology, and so on.

ACKNOWLEDGMENTS

This work was supported by the National Key R&D Program of China (Grant No. 2020YFA0211400) and the Opening Project of the Key Lab of Health Informatics of the Chinese Academy of Sciences (Grant No. 2011DP173015-2020-1). Z. S. and D. Z. thank Mr. Xinchao Song for the helpful suggestion.

[1] J. F. Nye and M. V. Berry, Dislocations in wave trains, Proc. R. Soc. London, Ser. A **336**, 165 (1974).

[2] B. T. Hefner and P. L. Marston, Acoustical helicoidal waves and Laguerre-Gaussian beams: Applications to scattering and to angular momentum transport, J. Acoust. Soc. Am **103**, 2971 (1998).

[3] B. T. Hefner and P. L. Marston, An acoustical helicoidal wave transducer with applications for the alignment of ultrasonic and underwater systems, J. Acoust. Soc. Am. **106**, 3313 (1999).

[4] S. T. Kang and C. K. Yeh, Potential-well model in acoustic tweezers, IEEE Trans. Ultrason. Ferroelectr. Freq. Control **57**, 1451 (2010).

[5] A. Marzo, S. A. Seah, B. W. Drinkwater, D. R. Sahoo, B. Long, and S. Subramanian, Holographic acoustic elements for manipulation of levitated objects, Nat. Commun. **6**, 8661 (2015).

[6] C. R. Courtney, C. E. Demore, H. Wu, A. Grinenko, P. D. Wilcox, S. Cochran, and B. W. Drinkwater, Independent trapping and manipulation of microparticles using dexterous acoustic tweezers, Appl. Phys. Lett. **104**, 154103 (2014).

[7] D. Baresch, J. L. Thomas, and R. Marchiano, Observation of a single-beam gradient force acoustical trap for elastic particles: Acoustical tweezers, Phys. Rev. Lett. **116**, 024301 (2016).

[8] P. Liu, D. Ming, C. S. Tan, and B. Lin, Acoustic trapping with 3-D manipulation, Appl. Acoust. **155**, 216 (2019).

[9] M. Baudoin, J.-L. Thomas, R. A. Sahely, J.-C. Gerbedoen, Z. Gong, A. Sivery, O. B. Matar, N. Smagin, P. Favreau, and A. Vlandas, Spatially selective manipulation of cells with single-beam acoustical tweezers, Nat. Commun. **11**, 4244 (2020).

[10] N. Jiménez, V. Romero-García, L. M. García-Raffi, F. Camarena, and K. Staliunas, Sharp acoustic vortex focusing by Fresnel-spiral zone plates, Appl. Phys. Lett. **112**, 204101 (2018).

[11] S. Guo, X. Wang, X. Guo, Z. Ya, P. Wu, A. Bouakaz, and M. Wan, Decreased clot debris size and increased efficiency of acoustic vortex assisted high intensity focused ultrasound thrombolysis, J. Appl. Phys. **128**, 094901 (2020).

[12] M. Baudoin, J.-C. Gerbedoen, A. Riaud, O. B. Matar, N. Smagin, and J.-L. Thomas, Folding a focalized acoustical vortex on a flat holographic transducer: Miniaturized selective acoustical tweezers, Sci. Adv. **5**, eaav1967 (2019).

[13] W.-C. Lo, C.-H. Fan, Y.-J. Ho, C.-W. Lin, and C.-K. Yeh, Tornado-inspired acoustic vortex tweezer for trapping and manipulating microbubbles, Proc. Natl. Acad. Sci. U. S. A. **118**, e2023188118 (2021).

[14] M. A. Ghanem, A. D. Maxwell, Y.-N. Wang, B. W. Cunitz, V. A. Khokhlova, O. A. Sapozhnikov, and M. R. Bailey, Noninvasive acoustic manipulation of objects in a living body, Proc. Natl. Acad. Sci. U. S. A. **117**, 16848 (2020).

[15] M. A. Ghanem, A. D. Maxwell, O. A. Sapozhnikov, V. A. Khokhlova, and M. R. Bailey, Quantification of acoustic radiation forces on solid objects in fluid, Phys. Rev. Appl. **12**, 044076 (2019).

[16] A. Marzo, M. Caleap, and B. W. Drinkwater, Acoustic virtual vortices with tunable orbital angular momentum for trapping of Mie particles, Phys. Rev. Lett. **120**, 044301 (2018).

[17] K. Skeldon, C. Wilson, M. Edgar, and M. Padgett, An acoustic spanner and its associated rotational Doppler shift, New J. Phys. **10**, 013018 (2008).

[18] K. Volke-Sepulveda, A. O. Santillan, and R. R. Boullosa, Transfer of angular momentum to matter from acoustical

vortices in free space, Phys. Rev. Lett. **100**, 024302 (2008).
[19] A. O. Santillán and K. Volke-Sepúlveda, A demonstration of rotating sound waves in free space and the transfer of their angular momentum to matter, Am. J. Phys. **77**, 209 (2009).
[20] C. E. Demore, Z. Yang, A. Volovick, S. Cochran, M. P. MacDonald, and G. C. Spalding, Mechanical evidence of the orbital angular momentum to energy ratio of vortex beams, Phys. Rev. Lett. **108**, 194301 (2012).
[21] L. Ye, C. Qiu, J. Lu, K. Tang, H. Jia, M. Ke, S. Peng, and Z. Liu, Making sound vortices by metasurfaces, AIP Adv. **6**, 085007 (2016).
[22] J. Liu, Z. Li, Y. Ding, A. Chen, B. Liang, J. Yang, J. C. Cheng, and J. Christensen, Twisting linear to orbital angular momentum in an ultrasonic motor, Adv. Mater. **34**, 2201575 (2022).
[23] Z. Hong, J. Zhang, and B. W. Drinkwater, Observation of orbital angular momentum transfer from Bessel-shaped acoustic vortices to diphasic liquid-microparticle mixtures, Phys. Rev. Lett. **114**, 214301 (2015).
[24] T. Wang, M. Ke, W. Li, Q. Yang, C. Qiu, and Z. Liu, Particle manipulation with acoustic vortex beam induced by a brass plate with spiral shape structure, Appl. Phys. Lett. **109**, 123506 (2016).
[25] Z. Hong, J. Yin, W. Zhai, N. Yan, W. Wang, J. Zhang, and B. W. Drinkwater, Dynamics of levitated objects in acoustic vortex fields, Sci. Rep. **7**, 7093 (2017).
[26] R. Zhang, H. Guo, W. Deng, X. Huang, F. Li, J. Lu, and Z. Liu, Acoustic tweezers and motor for living cells, Appl. Phys. Lett. **116**, 123503 (2020).
[27] L. Zhang and P. L. Marston, Acoustic radiation torque on small objects in viscous fluids and connection with viscous dissipation, J. Acoust. Soc. Am. **136**, 2917 (2014).
[28] A. D. Maxwell, M. Bailey, B. W. Cunitz, M. Terzi, A. Nikolaeva, S. Tsysar, and O. A. Sapozhnikov, Vortex beams and radiation torque for kidney stone management, J. Acoust. Soc. Am. **139**, 2040 (2016).
[29] X. Jiang, B. Liang, J. C. Cheng, and C. W. Qiu, Twisted acoustics: Metasurface-enabled multiplexing and demultiplexing, Adv. Mater. **30**, e1800257 (2018).
[30] C. Zhang, X. Jiang, J. He, Y. Li, and D. Ta, Spatiotemporal acoustic communication by a single sensor via rotational Doppler effect, Adv. Sci. **10**, e2206619 (2023).
[31] X. R. Li, D. J. Wu, Y. C. Luo, J. Yao, and X. J. Liu, Coupled focused acoustic vortices generated by degenerated artificial plates for acoustic coded communication, Adv. Mater. Technol. **7**, 2200102 (2022).
[32] H. Zhang and J. Yang, Transmission of video image in underwater acoustic communication, arXiv preprint arXiv:1902.10196 (2019).
[33] C. Shi, M. Dubois, Y. Wang, and X. Zhang, High-speed acoustic communication by multiplexing orbital angular momentum, Proc. Natl. Acad. Sci. U. S. A. **114**, 7250 (2017).
[34] J. L. Thomas and R. Marchiano, Pseudo angular momentum and topological charge conservation for nonlinear acoustical vortices, Phys. Rev. Lett. **91**, 244302 (2003).
[35] R. Marchiano and J. L. Thomas, Synthesis and analysis of linear and nonlinear acoustical vortices, Phys. Rev. E **71**, 066616 (2005).
[36] B. T. Hefner and B. R. Dzikowicz, A spiral wave front beacon for underwater navigation: basic concept and modeling, J. Acoust. Soc. Am. **129**, 3630 (2011).
[37] N. Jiménez, J. Ealo, R. D. Muelas-Hurtado, A. Duclos, and V. Romero-García, Subwavelength acoustic vortex beams using self-demodulation, Phys. Rev. Appl. **15**, 054027 (2021).
[38] S. Wang, G. Ma, and C. T. Chan, Topological transport of sound mediated by spin-redirection geometric phase, Sci. Adv. **4**, eaaq1475 (2018).
[39] F. Liu, W. Li, Z. Pu, and M. Ke, Acoustic waves splitter employing orbital angular momentum, Appl. Phys. Lett. **114**, 193501 (2019).
[40] S. Gspan, A. Meyer, S. Bernet, and M. Ritsch-Marte, Optoacoustic generation of a helicoidal ultrasonic beam, J. Acoust. Soc. Am. **115**, 1142 (2004).
[41] J. L. Ealo, J. C. Prieto, and F. Seco, Airborne ultrasonic vortex generation using flexible ferroelectrets, IEEE Trans. Ultrason. Ferroelectr. Freq. Control **58**, 1651 (2011).
[42] X. Jiang, Y. Li, B. Liang, J. C. Cheng, and L. Zhang, Convert acoustic resonances to orbital angular momentum, Phys. Rev. Lett. **117**, 034301 (2016).
[43] S.-W. Fan, Y.-F. Wang, L. Cao, Y. Zhu, A.-L. Chen, B. Vincent, B. Assouar, and Y.-S. Wang, Acoustic vortices with high-order orbital angular momentum by a continuously tunable metasurface, Appl. Phys. Lett. **116**, 163504 (2020).
[44] J. J. Liu, B. Liang, J. Yang, J. Yang, and J. C. Cheng, Generation of non-aliased two-dimensional acoustic vortex with enclosed metasurface, Sci. Rep. **10**, 3827 (2020).
[45] X. Jiang, J. Zhao, S.-l. Liu, B. Liang, X.-y. Zou, J. Yang, C.-W. Qiu, and J.-c. Cheng, Broadband and stable acoustic vortex emitter with multi-arm coiling slits, Appl. Phys. Lett. **108**, 203501 (2016).
[46] N. Jiménez, V. Sánchez-Morcillo, R. Pico, L. M. Garcia-Raffi, V. Romero-Garcia, and K. Staliunas, High-order acoustic Bessel beam generation by spiral gratings, Phys. Procedia **70**, 245 (2015).
[47] N. Jiménez, R. Picó, V. Sanchez-Morcillo, V. Romero-Garcia, L. M. Garcia-Raffi, and K. Staliunas, Formation of high-order acoustic Bessel beams by spiral diffraction gratings, Phys. Rev. E **94**, 053004 (2016).
[48] H. Zhou, J. Li, K. Guo, and Z. Guo, Generation of acoustic vortex beams with designed Fermat's spiral diffraction grating, J. Acoust. Soc. Am. **146**, 4237 (2019).
[49] D.-C. Chen, Q.-X. Zhou, X.-F. Zhu, Z. Xu, and D.-J. Wu, Focused acoustic vortex by an artificial structure with two sets of discrete Archimedean spiral slits, Appl. Phys. Lett. **115**, 083501 (2019).
[50] S. Jiménez-Gambín, N. Jiménez, J. M. Benlloch, and F. Camarena, Generating Bessel beams with broad depth-of-field by using phase-only acoustic holograms, Sci. Rep. **9**, 20104 (2019).
[51] S. Jiménez-Gambín, N. Jiménez, and F. Camarena, Transcranial focusing of ultrasonic vortices by acoustic holograms, Phys. Rev. Appl. **14**, 054070 (2020).
[52] A. S. Pilipchuk, A. A. Pilipchuk, and A. F. Sadreev, Generation of vortex waves in noncoaxial cylindrical waveguides, J. Acoust. Soc. Am. **146**, 4333 (2019).
[53] T. Liu, S. An, Z. Gu, S. Liang, H. Gao, G. Ma, and J. Zhu, Chirality-switchable acoustic vortex emission via

non-Hermitian selective excitation at an exceptional point, Sci. Bull. **67**, 1131 (2022).

[54] H. Zhang, Y. Sun, J. Huang, B. Wu, Z. Yang, K. Y. Bliokh, and Z. Ruan, Topologically crafted spatiotemporal vortices in acoustics, Nat. Commun. **14**, 6238 (2023).

[55] H. Ge, S. Liu, X.-Y. Xu, Z.-W. Long, Y. Tian, X.-P. Liu, M.-H. Lu, and Y.-F. Chen, Spatiotemporal acoustic vortex beams with transverse orbital angular momentum, Phys. Rev. Lett. **131**, 014001 (2023).

[56] H. E. Hartig and C. E. Swanson, "Transverse" acoustic waves in rigid tubes, Phys. Rev. **54**, 618 (1938).

[57] M. Bruneau, *Fundamentals of Acoustics* (John Wiley & Sons, Hoboken, New Jersey, USA, 2013).

[58] F. Jacobsen and P. M. Juhl, *Fundamentals of General Linear Acoustics* (John Wiley & Sons, Hoboken, New Jersey, USA, 2013).

[59] A. S. Pilipchuk, A. A. Pilipchuk, and A. F. Sadreev, Multi-channel bound states in the continuum in coaxial cylindrical waveguide, Phys. Scr. **94**, 115004 (2019).

[60] See Supplemental Material at http://link.aps.org/supplemental/10.1103/PhysRevApplied.21.064006 for (S1) higher-order eigenmodes for cylinder waveguide with circle cross-section and gradient sawtooth metasurface, (S2) verifying the analytical expressions of eigenmodes $|p_1\rangle$ and $|p_2\rangle$, and (S3) controlling the weights of the two eigenmodes $|p_1\rangle$ and $|p_2\rangle$ through tuning the position of the sound source, which includes Refs. [33,52,59,61,62].

[61] D. N. Maksimov, A. F. Sadreev, A. A. Lyapina, and A. S. Pilipchuk, Coupled mode theory for acoustic resonators, Wave Motion **56**, 52 (2015).

[62] A. Lyapina, A. Pilipchuk, and A. Sadreev, Trapped modes in a non-axisymmetric cylindrical waveguide, J. Sound Vib. **421**, 48 (2018).

[63] Z. Hou, H. Ding, N. Wang, X. Fang, and Y. Li, Acoustic vortices via nonlocal metagratings, Phys. Rev. Appl. **16**, 014002 (2021).

[64] J. Lekner, Acoustic beams with angular momentum, J. Acoust. Soc. Am. **120**, 3475 (2006).

[65] L. Zhang and P. L. Marston, Angular momentum flux of nonparaxial acoustic vortex beams and torques on axisymmetric objects, Phys. Rev. E **84**, 065601 (2011).